Inkjet-/3D-/4D-Printed Perpetual Electronics and Modules
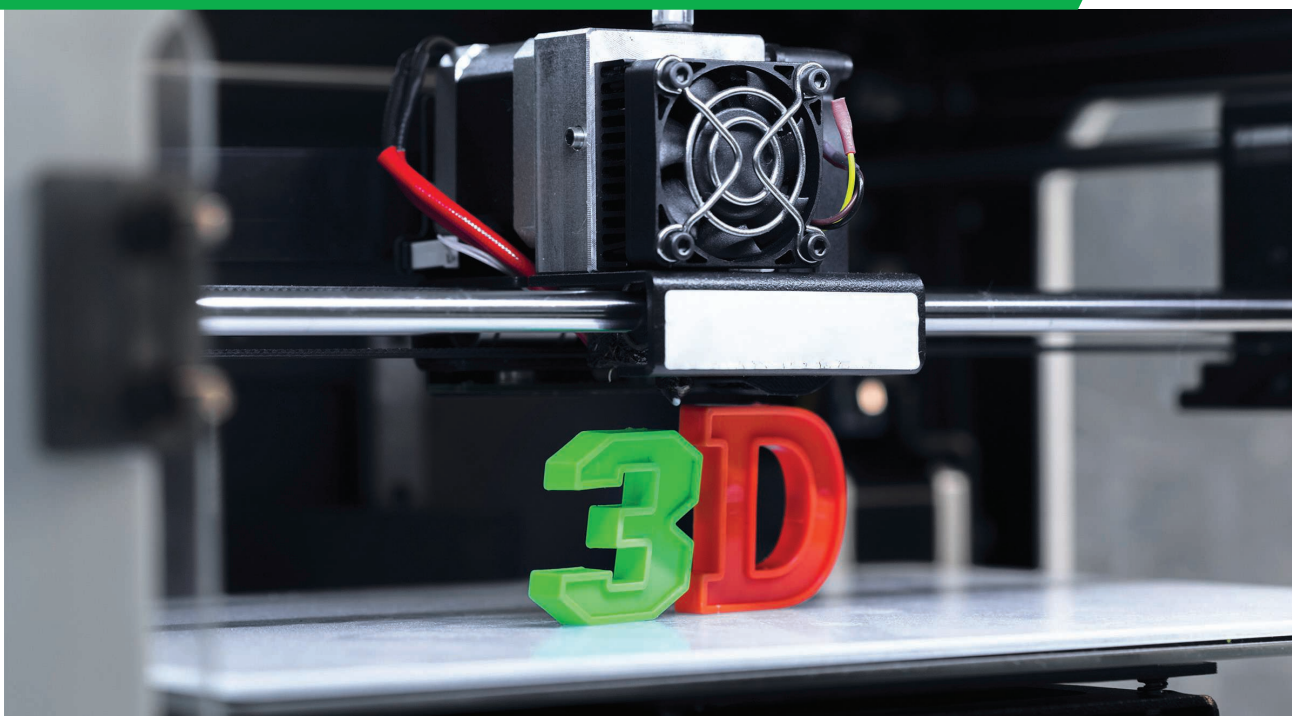
*Aline Eid, Xuanke He,
Ryan Bahr, Tong-Hong Lin,
Yepu Cui, Ajibayo Adeyeye,
Bijan Tehrani, and
Manos M. Tentzeris*

With the revolutionary developments in the fields of millimeter-wave (mm-wave) and Internet of Things (IoT) technologies and the billion devices promised to be implemented by the end of the decade, the realization of inexpensive, low-power, and intelligent systems is highly desirable. Additive manufacturing (AM) is a technology seeing widespread adoption due to its ability to enable rapid prototyping for iterative design; its reduced setup costs, facilitating economic small-batch production; and its ability to significantly reduce

waste by-products, resulting in both environmental benefits as well as lower manufacturing costs. On the other hand, current lithography-based manufacturing technologies—a huge contributor to the growing RF and 5G wireless electronics industry—require extensive design verification, have longer turnaround times, and produce harmful byproducts. Although AM can offer time and cost benefits under the correct conditions, among the more impactful demonstrations of the manufacturing technology are the novel topologies enabled by design rules that allow feature sets, including nonorthogonal planes, conformal surfaces, multimaterial deposition, simultaneous thick- and thin-film deposition [1], complex 3D structures, integrated voids, and gradient index materials.

Research toward the development of flexible electronics is very active at all levels, from the physical characterization of printed materials at the component level and the development and improvement of printed interconnects at the chip and die levels to the integration of such components into fully printed flexible systems, such as flexible displays and wearable and portable devices [2]. This review article shows how inkjet and 3D printing are used to develop the different functions that make up a typical IoT wireless sensor module: communications, sensing, and powering. In addition, inkjet and 3D printing unlock the use of two additional dimensions and the introduction of features otherwise unattainable using conventional manufacturing processes. Those two added dimensions are the result of the additional degree of mechanical freedom enabled by 3D printing relative to planar printed circuit board manufacturing, while the fourth dimension, known as *4D*, is from dynamic structures where the structure changes shape in a controlled manner that offers reconfigurability and tunability for mm-wave systems.

First, we present cutting-edge packaging techniques, such as system in package (SiP), system on package (SoP), and smart module encapsulation enabled on a variety of substrates, demonstrating performance superiority over traditional packaging methods. These manufacturing techniques are also demonstrated to enable unique features such as origami-based RF and microwave solutions, offering a combination of reconfigurability, low cost, ease of fabrication, and flexibility. Moreover, uniquely featured mm-wave harvester and RFID tag architectures based on a Rotman lens for the

realization of ultralong-range 5G-enabled harvesting and low-power communications allow for the implementation of compact, fully printed power-autonomous RFID tags for ultra-accurate mm-wave spatial localization and sensing applications (see Figure 1). The various designs demonstrate significant advances that begin at the packaging level, progress to unique mm-wave components, and can be further extended into novel innovative systems that enable low-cost solutions to power the next generation of IoT devices expected in 5G communication systems.

Novel mm-Wave Packaging For Next-Generation Interconnects Using AM

The performance, range, and throughput of an mm-wave system are dependent not only on continuous advances of the semiconductor devices themselves but on every component in between. Every decibel of performance improvement spread across the various elements of a circuit will aggregate and have significant impacts on the deployment range and data throughput of distributed networks. Monolithic microwave integrated circuits (MMICs) use various topologies to limit the parasitics from interconnects, which adversely impact the bandwidth (BW) and insertion loss of integrated devices and cascaded components in 5G systems. Some works featuring additive manufactured packaging of mm-wave/high-frequency devices have utilized aerosol jet printing, such as those in [3] and [4]. Although aerosol jet printing offers an increased printing resolution, it is costlier to operate and utilizes only a few printing nozzles compared to the thousands available on a commercial inkjet printhead, making aerosol less suitable for large-scale production settings. Other works, such as those presented in [5] and [6], rely on a hybrid additive process called *rapid microproduct development* (*RMPD*), which features a 110–170-GHz D-band integration. However, the use of masking and lithography in RMPD negates some AM advantages that are preserved with inkjet printing, which is fully additive and an easily scalable solution.

Inkjet printing has shown the ability to decrease the losses of interconnects at mm-wave frequencies compared to traditional RF ribbon-bond interconnects, which have a long loop length, large parasitic inductance at high frequencies, and greater discontinuities [7]. With MMIC embedded into a cavity, a dielectric filler can be printed, acting as a smooth

Aline Eid (aeid7@gatech.edu), Xuanke He (xhe53@gatech.edu), Ryan Bahr (rbahr3@gatech.edu), Tong-Hong Lin (thlin@gatech.edu), Yepu Cui (yepu.cui@gatech.edu), Ajibayo Adeyeye, Bijan Tehrani (btehrani3@gatech.edu), and Manos M. Tentzeris (etentze@ece.gatech.edu) are with the School of Electrical and Computer Engineering, Georgia Institute of Technology, Atlanta, United States.

transition for the mm-wave, inkjet-printed interconnect, which more closely resembles an ideal, continuous transmission line. The impact of the improved performance of inkjet-printed interconnects is demonstrated against traditional ribbon bonds, as demonstrated in Figure 2(a) and (b).

Three different test vehicles were fabricated to evaluate this novel packaging technique for active devices. An Analog Devices ALH369 low-noise amplifier (LNA) operating at mm-wave frequencies had inkjet-printed interconnects manufactured, connecting the die to 50 Ω, with two fabricated to evaluate the consistency. Using the same evaluation board, two ribbon-bonded LNA samples were fabricated and used as a test benchmark against the mm-wave inkjet-printed samples, with the results shown in Figure 2(e). The inkjet-printed samples exhibited a superior $|S_{21}|$ performance throughout the whole operation range

up to 40 GHz with a peak improved gain of 3.3 dB for a Ka-band LNA.

A fully functioning multichip module (MCM) was demonstrated as the next iteration of this inkjet-printing interconnect technology [8]. The MCM front-end module consists of an LNA, a power amplifier (PA), and switch MMICs that are packaged using the same technique. The ALH369 LNA was used as the receiver (Rx) IC, the TGA4036 was used as the transmitter (Tx) IC, and the TGS4302 was used as the switching module between the Tx/Rx and the shared output port, allowing for time-domain duplexing within the MCM. All packaging is done in a fully additive fashion. Instead of a copper circuit board interface, the entire circuit board conductor layer was inkjet-printed on Rogers 4003 C. As displayed in Figure 3, the LNA and PA both turned on and provided gain, which was nominally around 3.5 to 4 dB below the bare die measurements. This takes
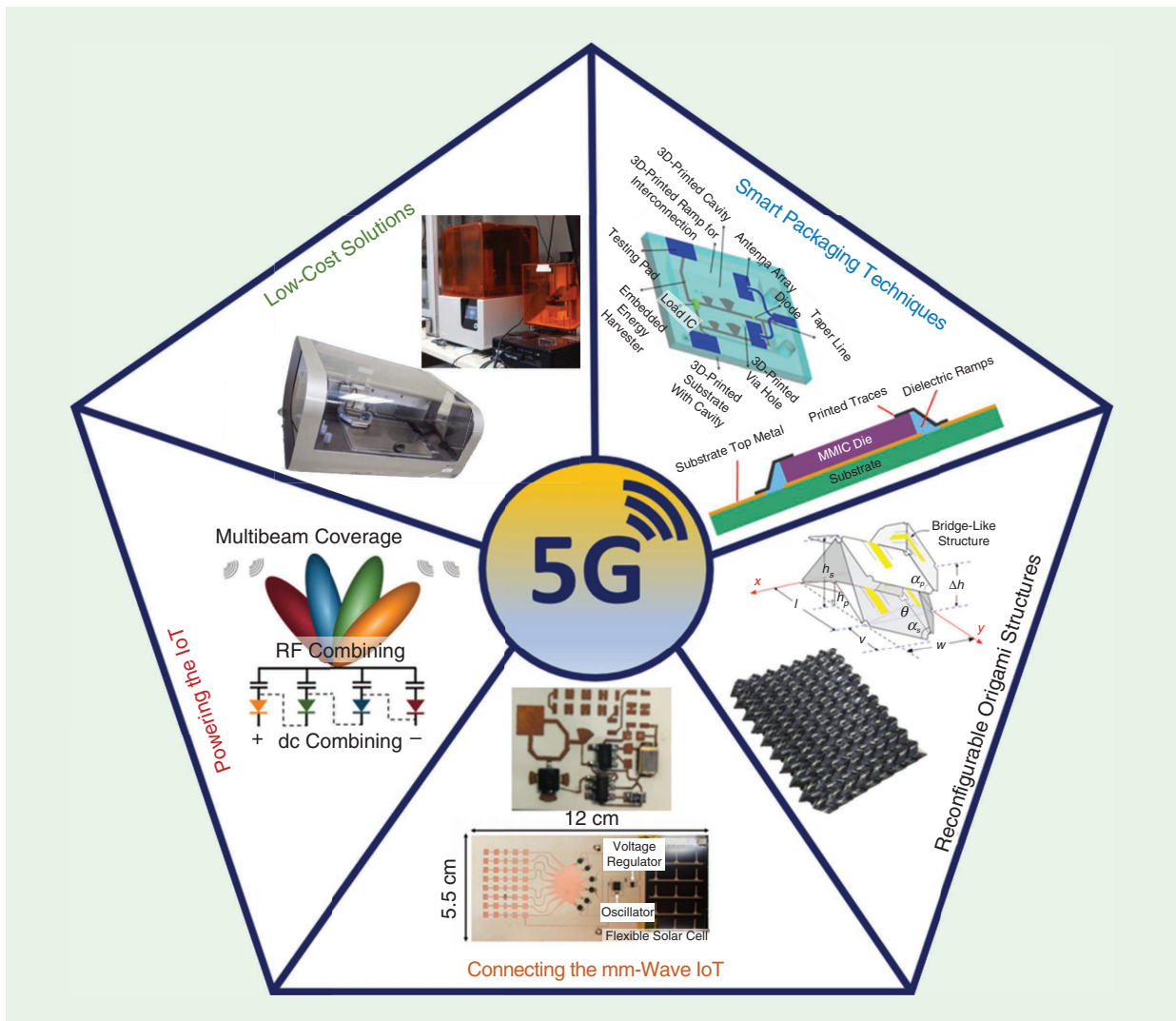

Figure 1. An overview of the wide range of 5G-enabled wireless electronics manufactured using low-cost AM techniques. MMIC: monolithic microwave integrated circuit.

into account the losses between the switch MMIC and additional chip-to-chip (PA to switch, switch to LNA) interconnects as well as the transmission line and connector port losses.

To protect the MMICs from environmental or physical damage, they are typically encapsulated with a plastic overmold and typically offer no additional features. AM, however, can enable the use of "smart" packaging, which adds additional features to the MCM. The nature of the AM method allows for a straightforward incorporation of smart features on the encapsulation structure. A circular-ring frequency selective surface (FSS) was designed at 24 GHz to block out interference in this band of interest, and a 3D-printed encapsulation has an air cavity to reduce dielectric loading on the ICs. The FSS is then inkjet-printed on top of this encapsulation structure using its drop-on-demand feature that deposits silver nanoparticle ink only where
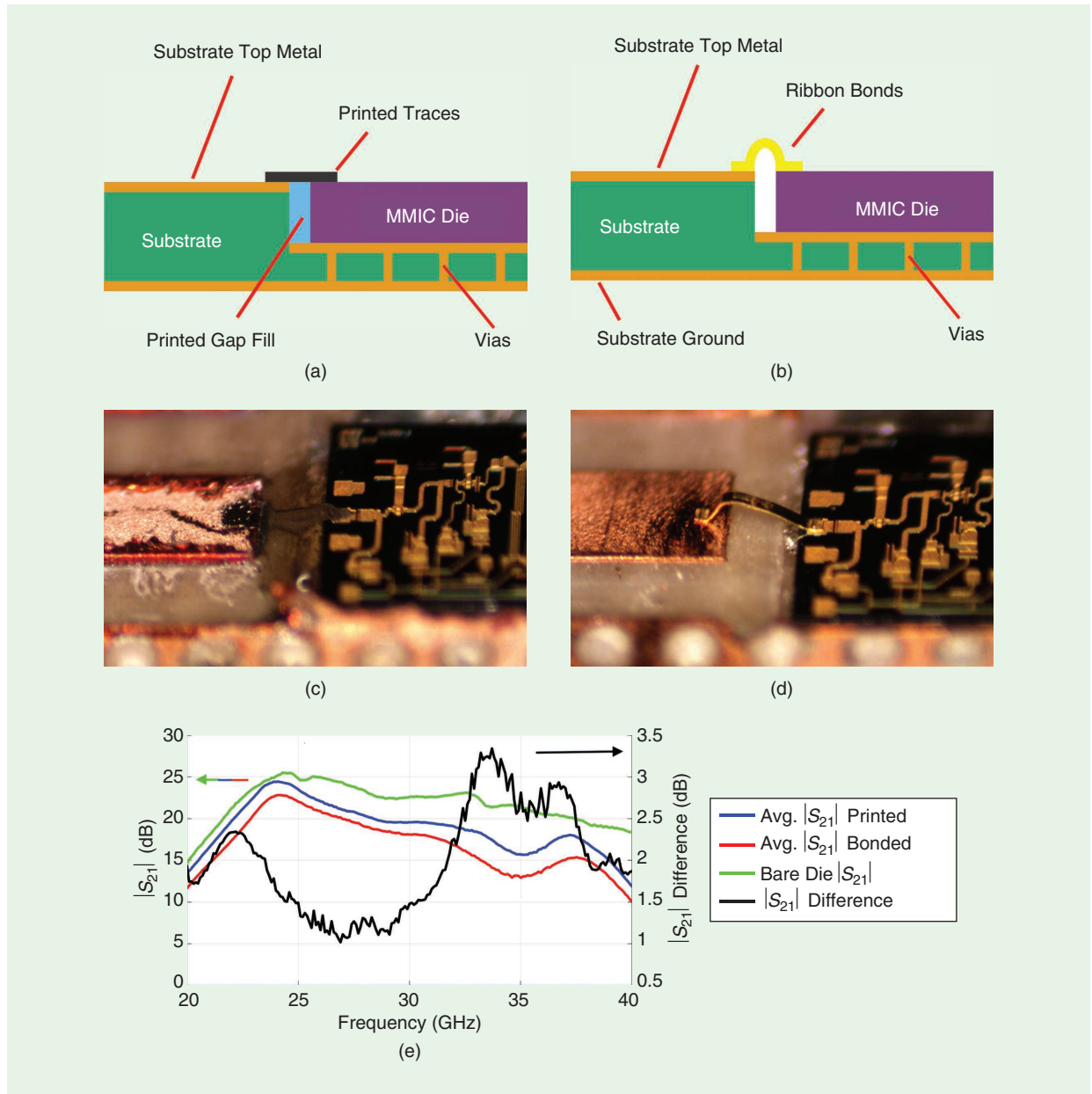

Figure 2. *A summary of the side-view schematics of the printed gap-filled interconnect topologies discussed. A comparison between (a) an mm-wave inkjet-printed interconnect and (b) a ribbon-bond interconnect, with the implementation of each shown in (c) and (d), respectively. (e) The average insertion loss for printed and bonded samples (left y-axis) and the difference in insertion loss between printed and bonded samples (right y-axis). The bare die measurement is shown as a reference [8]. Avg.: average.*

it is needed, reducing waste and processing time. The fabricated 3D-printed encapsulant on top of the MCM is shown in Figure 4.

Figure 5 shows the data collected from the measurement setup during pre- and postencapsulation. Prior to encapsulation, the bare die MCM observed poor electromagnetic interference (EMI) shielding, as the LNA amplified the incoming interference signal with only roughly a −20-dBi signal transmission from the interference antenna to the output of the LNA in this
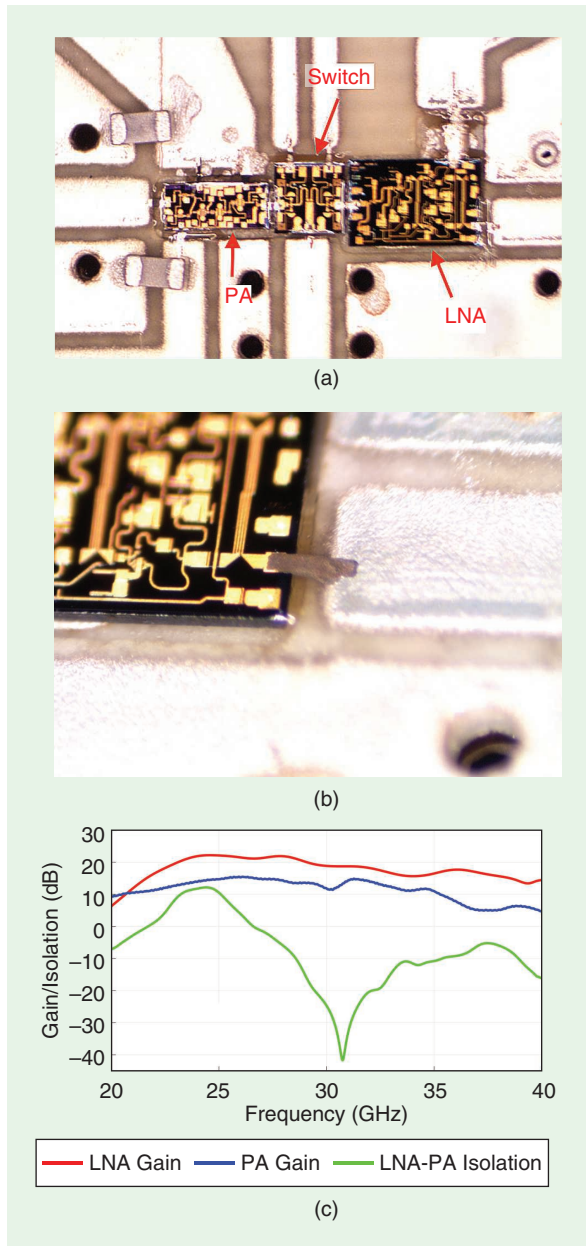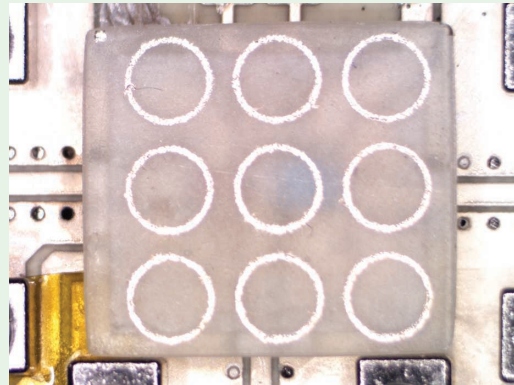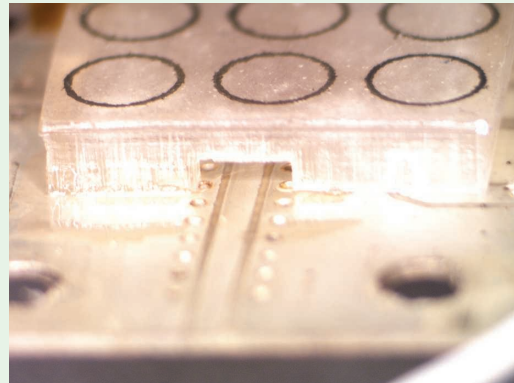

(a)

(b)

(c)

Figure 3. (a) A full MCM mm-wave front end with PAs, LNAs, and switch MMICs. (b) The perspective view of an mm-wave inkjet-printed interconnect. (c) The $|S_{21}|$ performance of the MCM [8].

(a)

(b)

Figure 4. (a) A 24-GHz FSS printed on top of the 3D-printed cavity encapsulation of the MCM. (b) A side-perspective view [8].
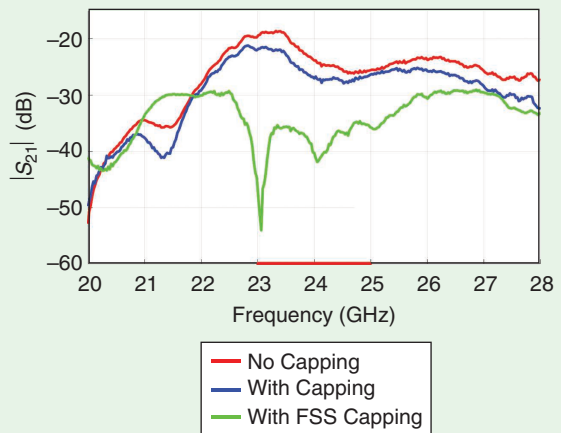

Figure 5. EMI measurements pre- and postencapsulation with the FSS, demonstrating a large increase in EMI isolation from the 23- to 25-GHz range [8].
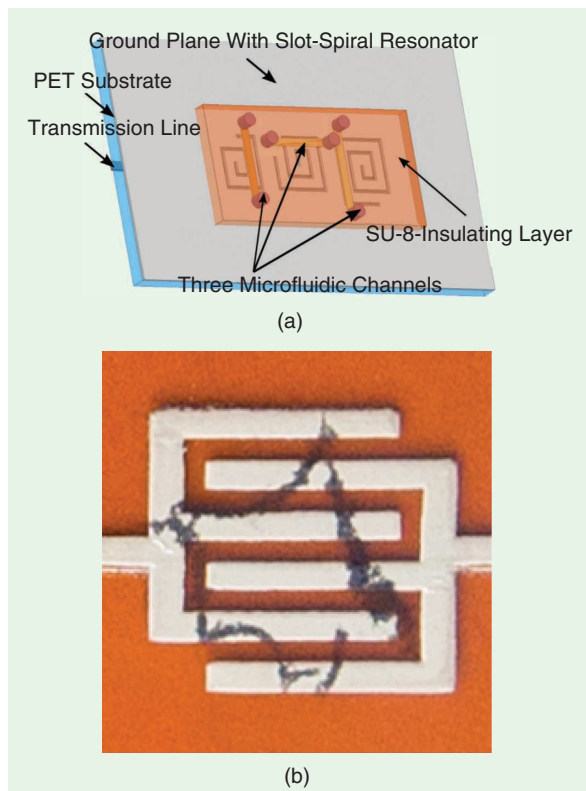
Figure 6. (a) A fully inkjet-printed microfluidic chipless RFID sensor design and (b) a chemical sensor printed using silver nanoparticles and carbon nanotubes inks [10]. PET: positron emission tomography.
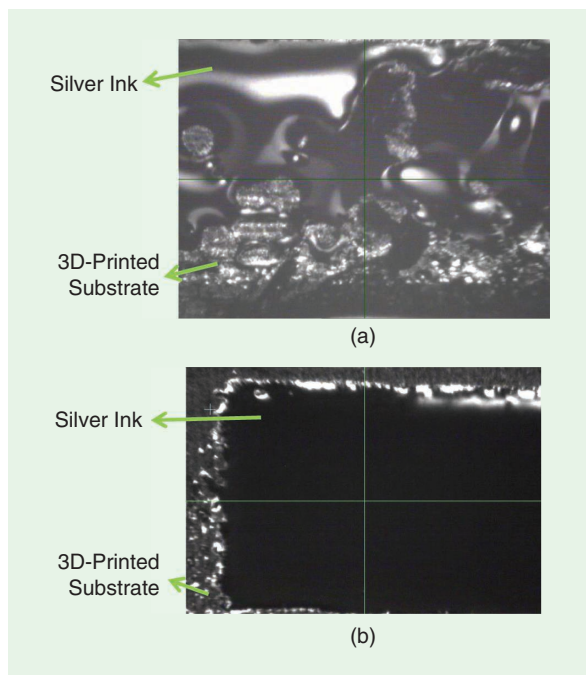

Figure 7. (a) Ink adhesion without surface treatment. (b) Ink adhesion after exposure to the UV ozone layer prior to inkjet printing [14].

test setup. Following the printing of the FSS on top of the encapsulant, an extra 18 dB or more of isolation was observed at 24 GHz, a large improvement from the bare die measurement, with no effect on the $|S_{21}|$ performance of the MCM. This enhances the capabilities of the module, providing features that improve EMI shielding and help with desense, and lays the groundwork for more advanced smart features to be incorporated into the packaging, including sensors or antennas. Figure 6 depicts an example of the design of a microfluidic sensor [9] and a chemical sensor [10] developed using fully inkjet-printed techniques. With the incorporation of those wireless sensors into the packaging, novel, low-cost self-monitoring and self-diagnostic capabilities will be enabled.

Perpetual 5G SoP Modules

What if the smart packaging discussed in the previous section could become a power source for the next generation of the IoT? Energy harvesting is one of the key enabling technologies to realize perpetual electronics. It can collect various energy such as solar, vibration, and RF waves from the surroundings and then convert it to usable dc power to drive electronic devices. As long as the surrounding energy sources are there, the electronics equipped with energy-harvesting technologies can maintain their operation. With the increased density of wireless Txs as each generation of wireless networks is deployed, the ability to utilize the widespread number of transceivers as a power source becomes both more appealing and realizable. Numerous RF energy-harvesting topologies have been proposed, including harvesting from handheld devices [11] and from ultrahigh-frequency (UHF) signals [12].

Recently, with the rise of the new 5G communication, interest in harvesting energy from mm-wave wireless signals has grown considerably, especially with the permitted higher-power emissions allowed by the U.S. Federal Communications Commission [up to 75-dBm effective isotropic radiated power (EIRP)]. To realize wireless energy harvesting, sources of the loss in the system must be minimized, including the high transmission line losses at mm-wave frequencies between energy-harvesting circuits, ICs, and antennas. SoP topology offers integrated passives such as antenna-in-package (AiP) designs and actives such as ICs in a small package that become a practical methodology for mm-wave energy harvesting [13].

With the advancement in AM capabilities such as lithographic processes and resolutions and in multimaterial printing, a new fabrication process is introduced in this section that is suitable for the realization of mm-wave circuits. A 5G AiP design realized with the introduced process is used as a proof-of-concept demonstration [14], [15]. Then, a perpetual 5G SoP module

with an integrated energy harvester implemented using multilayered AM technologies is demonstrated [13]. As this 5G SoP module can be functional without external energy sources or circuits, the size is shrunk to a package level, paving the way to large-scale, miniaturized IoT deployment.

Fully Printed 5G AiP Design

One key challenge to integrating both 3D and inkjet printing is the mechanical differences between dissimilar materials, including adhesion and various compatibility issues. As shown in Figure 7(a), the adhesion
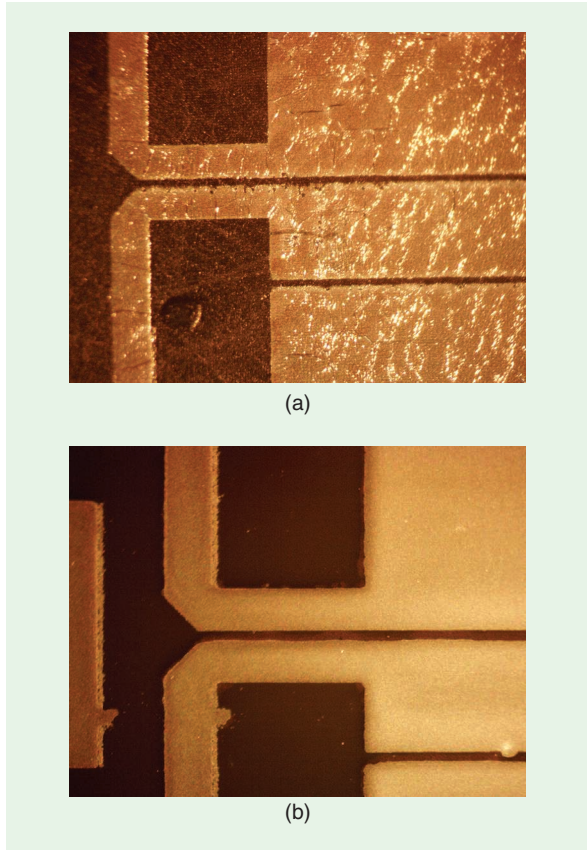
Figure 8. *Inkjet-printing results (a) without SU-8 coating and (b) with SU-8 coating [14].*

Figure 9. *An inkjet- and 3D-printed broadband AiP design [14].*

between inkjet-printed silver and a 3D-printed flexible substrate can critically affect the conductive layer when no surface treatment was applied. However, when the ultraviolet (UV) ozone surface treatment was applied, as depicted in Figure 7(b), the improvement to the silver ink becomes apparent. Additional constraints include the surface roughness of various 3D printing technologies, often magnitudes worse than inkjet printing, as well as the different coefficients of thermal expansion (CTE) between different materials. Due to this, microscopic cracks are inevitable after sintering the metallic layer, as illustrated in Figure 8. Although these cracks might be acceptable for low-frequency applications, they are detrimental to the performance for mm-wave applications. A solution is to deposit a buffer layer, consisting of one thin layer of SU-8 2000 polymer series by MicroChem (Newton, Massachusetts) [16]. This applied layer acts as a buffer to smooth the 3D-printed surface and improve the CTE differences between the 3D-printed substrate and inkjet-printed silver.
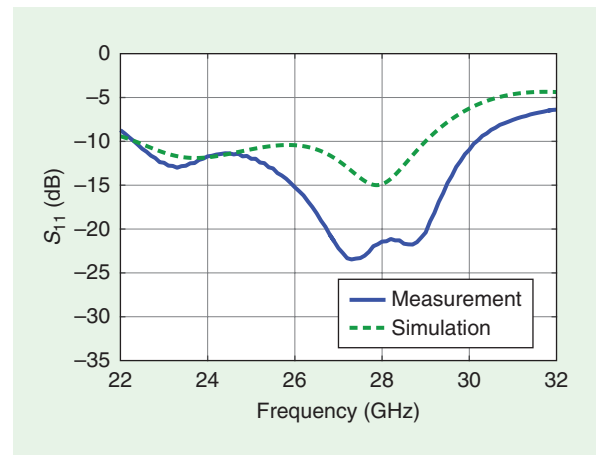
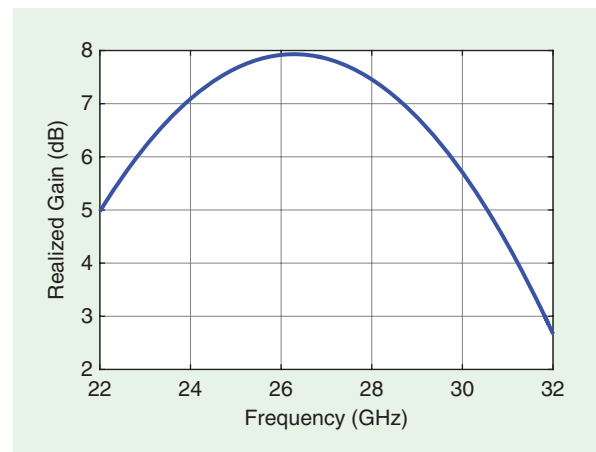**Figure 10.** *The measured and simulated S_{11} of the proposed AiP design [14].*

Figure 11. *The measured realized gain of the proposed AiP design [14].*

As presented in Figure 8, significant enhancement and elimination of all the cracks were observed after the adoption of the SU-8 buffer layer. With the UV ozone surface treatment and SU-8 buffer layer, inkjet and 3D printing can be coherently integrated in terms of the required resolution, surface roughness, and printing quality appropriate for mmwave applications.

The fabrication process is utilized to realize a 5G AiP design, as shown in Figure 9. The measured S_{11} and realized gain are displayed in Figures 10 and 11, respectively. The measured S_{11} is smaller than –10 dBi from 22.4 to 30.1 GHz, and the fractional BW is 29.3%. The measured realized gains are larger than 5 dBi from 22 to 30.5 GHz. The BW is broad enough to cover both 5G New Radio bands n257 (26.5–29.5 GHz) and n258 (24.25–27.5 GHz). The proof-of-concept AiP design validates that the proposed fabrication process can be applied to realize mmwave circuits with great quality and performance.

Compared to previous works, the AiP design can achieve broad BW with good gain. In [17], an AiP design using organic substrate was demonstrated. The realized BW was from 30 to 30.8 GHz, with a fractional BW of 2.6%. Other AiP designs for active modules were demonstrated in [18]–[20]. These three works used patch arrays in the package operating at 5G frequency bands, and the highest realized fractional BW was 13.3%.
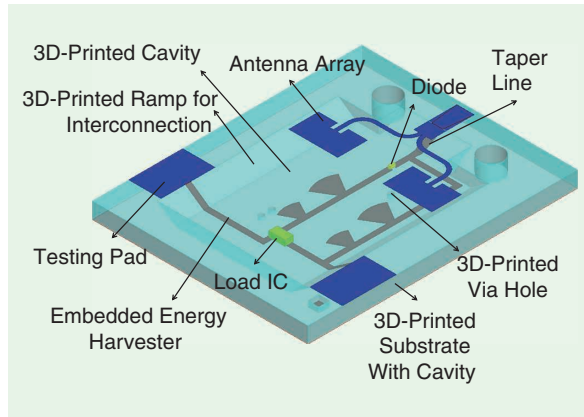
5G SoP Module

The topology of a perpetual 5G SoP module is exhibited in Figure 12. The entirety of the system was fabricated using the fully AM fabrication process discussed previously. The energy harvester harnessing energy from 5G signals was embedded inside a 3D-printed cavity to support perpetual functionality. The 3D-printed ramp and inkjet-printed tapered microstrip line on top of the ramp were used as interlayer connections between the energy harvester and the patch antenna array on the top layer to reduce parasitics. The rectangular patch antenna AiP design was printed right on top of the
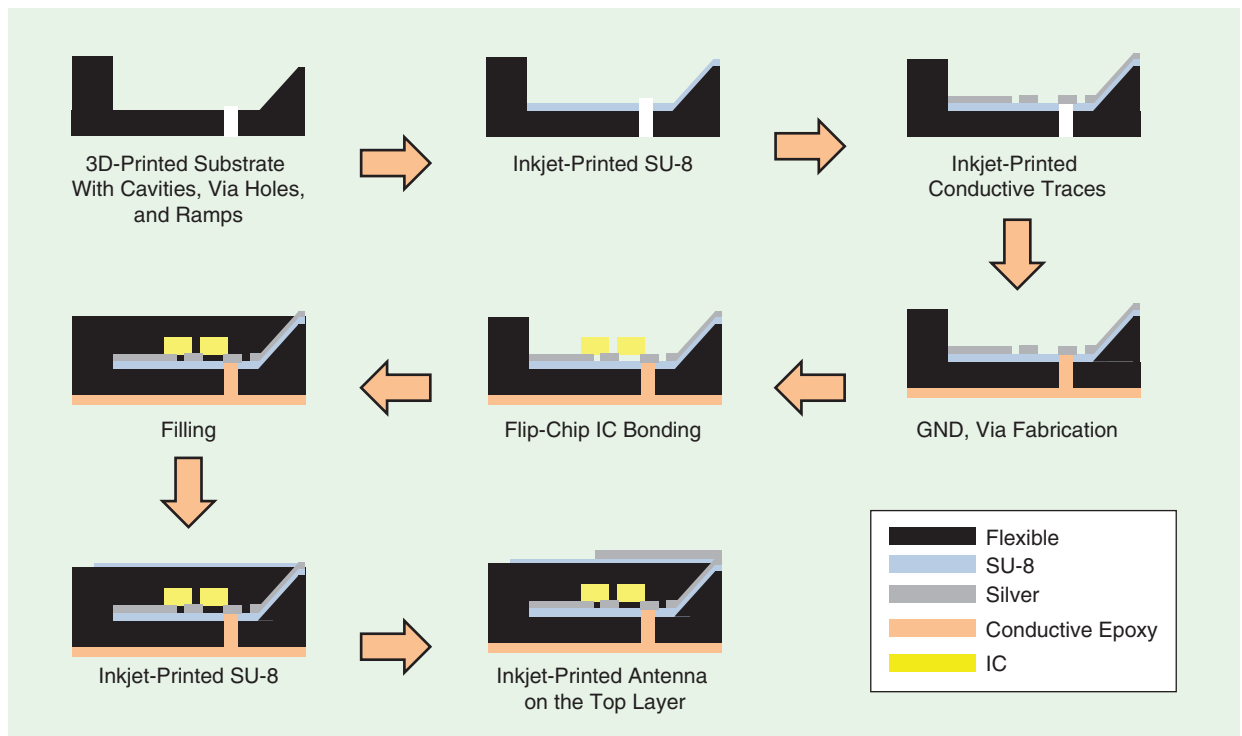
Figure 12. *The embedded-on-package energy harvester within a 3D-printed, multilayer packaging structure [13].*

Figure 13. *The fabrication process for multilayer printing [13]. GND: ground.*

energy harvester to reduce the overall transmission loss at mm-wave frequencies.

The multilayer fabrication process of the system is demonstrated in Figure 13. The first step was to 3D-print the flexible base substrate with ramps, vias, and a cavity using the Formlabs Form2 stereolithography 3D printer. The flexible substrate used was FLGR02 with a dielectric constant of 2.83 and a loss tangent of 0.03 at 26 GHz. The second step was to inkjet-print a thin layer of SU-8 to smooth the surface roughness of the 3D-printed substrate and buffer the CTE differences. The silver traces were inkjet-printed on the SU-8-coated substrate, as shown in Figure 14. The other side of the 3D-printed substrate was coated with conductive epoxy to create the ground plane, while the vias were also filled with conductive epoxy. The ICs were flip-chip bonded on the inkjet-printed silver traces with conductive epoxy, as displayed in Figure 14(b). The cavity was then filled with FLGR02 to create a new layer. As depicted in Figure 15(a), the filling is flat, and the interlayer connection is ready for the antenna array on the top layer. Finally, another SU-8 and patch AiP array were inkjet-printed on top, as presented in Figure 15(b).

The embedded energy harvester with a 750-kΩ load resistor was measured at 26 GHz, and the results are shown in Figure 16. The simulated results before the filling of the cavity—extracted from advanced design system harmonic balance simulation—are also included for comparison. It can be seen that the

(a)

(b)

Figure 15. (a) Filling the cavity with flexible material. (b) An inkjet-printed antenna array on the top layer [13].
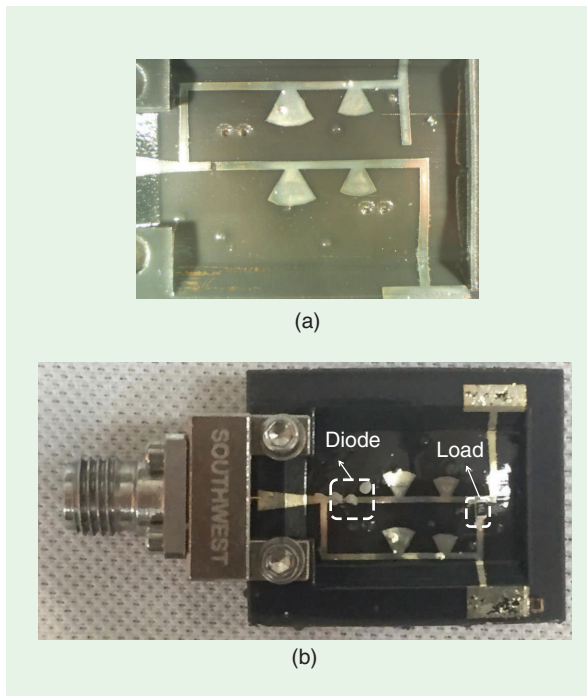

(a)

(b)

Figure 14. (a) Inkjet-printed silver on top of the 3D-printed substrate. (b) The package-integrated energy harvester [13].

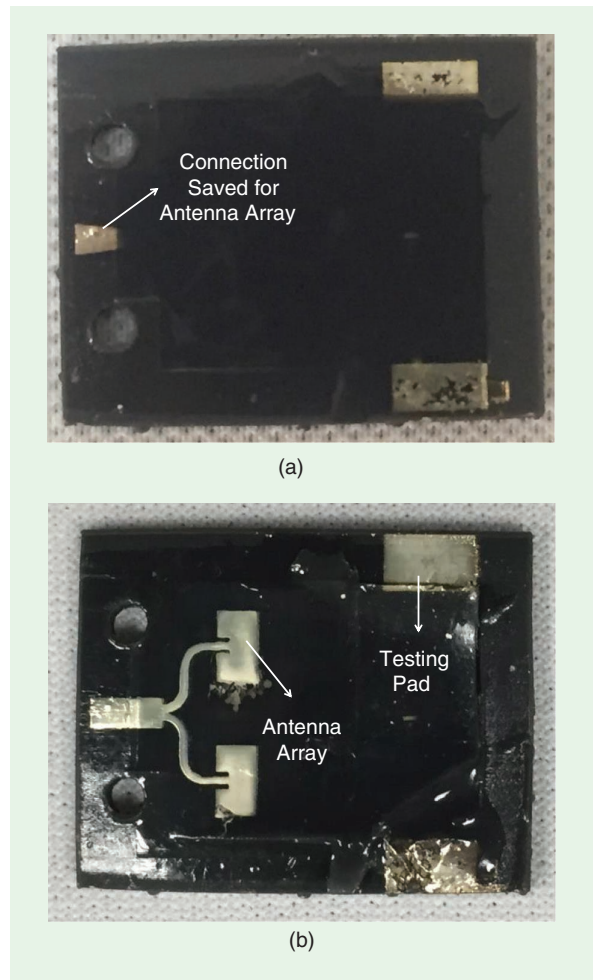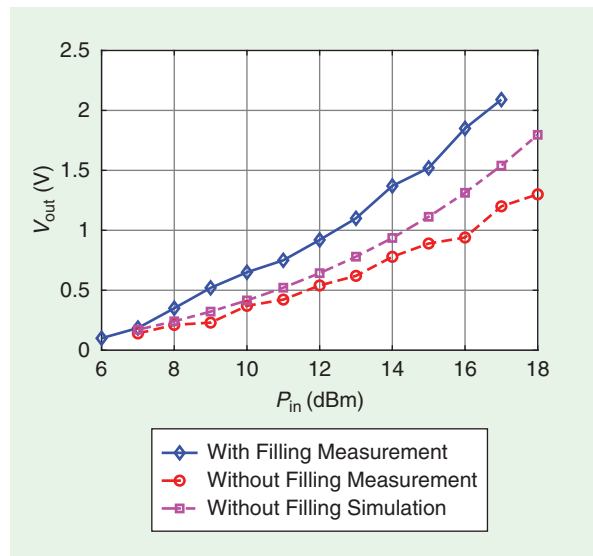**Figure 16.** The measured and simulated output voltages with respect to different input power at 26 GHz for the embedded energy harvester [13].

measured output voltage increases after filling the cavity; this is because the frequency shift occurring after filling the cavity was taken into consideration. Thus, the optimal operation point for the design before the filling is not at 26 GHz, but the optimal operational point after filling is at 26 GHz.

To measure the performance of the system, a signal generator's output is set to 12 dBm, with an amplifier of 27-dB gain and a horn antenna with a maximum gain of 20 dBi. The distance between the sample and the horn antenna is 20 cm, generating an output voltage at the load of the energy harvester of 0.9 V. Because the EIRP limit for 5G communication is approximately 75 dBm [21], the range can be extended to more than 1 m if the maximum EIRP is used. The measured harvested energy is powerful enough to drive a TS3001 timer from Silicon Labs, which can be used as the modulation control and a fully autonomous backscattering RFID module. This

5G SoP module can be functional perpetually without any exterior circuits or boards, thus reducing the fully functional system size from the board level down to the package level.

3D and 4D Printing for Origami-Inspired mm-Wave Structures

Although recent advancements have demonstrated novel approaches that increase the capability and decrease the size of IoT modules in the mm-wave spectrum, part of the advantage of AM technology is its scalability, making it applicable not only to electrically small structures but to very large ones as well. It can actually be utilized to demonstrate something in between: structures that change shape, enabling a component that can be both compact and large depending on the deployed state. This can be achieved with origami, the art of paper folding.

Origami-inspired RF designs featuring unprecedented capabilities for deployability and continuous-range tunability enable drastic improvements in the performance of devices such as antennas, sensors, filters, and so on. The integration of origami introduces an additional degree of freedom and reconfigurability to 3D structures—known as *4D*—through the use of multiple different tessellations. However, one key drawback of conventional origami-inspired RF devices is that they are commonly realized on paper-based substrate with a labor-intensive fabrication process [22], [23]. Even though paper is a good candidate for proof-of-concept prototypes, it is prone to absorbing moisture and tearing and also has significant dielectric losses. Moreover, the fabrication process requires manual cutting and folding; as a result, the accuracy is often insufficient for mm-wave applications.

Alternatively, origami-inspired RF structures can be realized on additively manufactured 3D-printed flexible substrates, which eliminates the requirement of folding and cutting and enables more complicated design elements such as slots, round holes, and more. Additionally, a fully automated, highly accurate additive printing process enables smaller-sized unit cells, opening the potential for 5G and mm-wave applications. A recent example of a 3D-printed, origami-inspired RF device is presented in [24] and uses a hybrid (3D and inkjet) printing fabrication process to realize a "shape-changing," reconfigurable mm-wave FDD. The design depicted in Figure 17(a) used a traditional Miura-Ori structure that can be folded along one axis by changing the folding angle *b*. The resonant frequency can be tuned from 21.6 to 24.9 GHz with a folding angle from 110 to 60°. The BW can be tuned from 14 to 32% by increasing the angle of incidence (AoI) from 0 to 60°. The three-step fabrication process shown in Figure 17(a) is
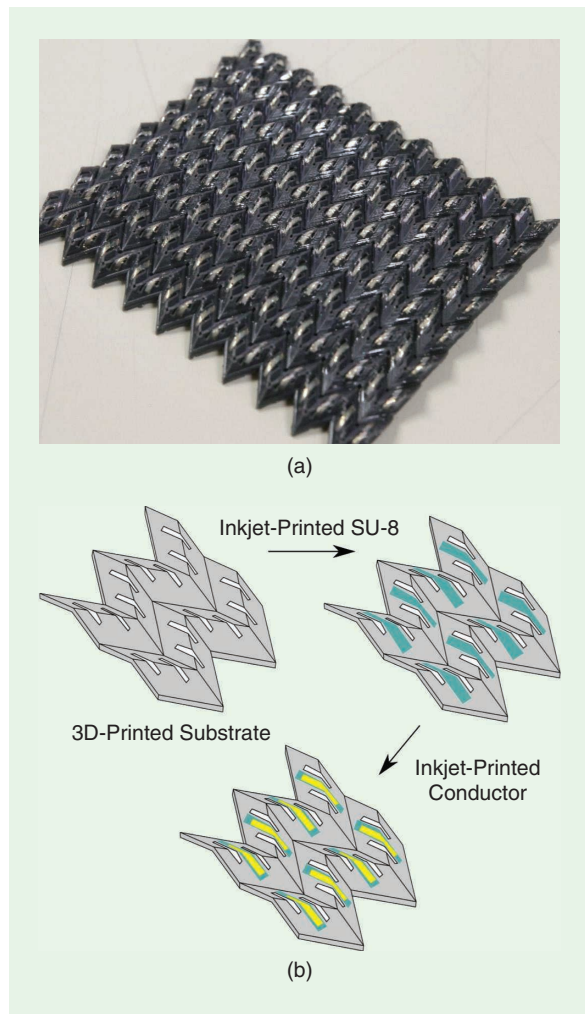

(a)

(b)

Figure 17. *The (a) prototype and (b) fabrication process of the hybrid-printed Miura-Ori mm-wave FSS [24].*

- 3D printing of a dielectric substrate
- inkjet printing of a thin SU-8 buffer layer to smooth out the substrate surface and improve conductive-layer adhesion
- inkjet printing of conductive layers and sintering with a low-temperature gradient.

Another advantage of 3D-printed, origami-inspired structures is to realize high-performance dielectric RF designs. Dielectric reflectarrays have drawn increasing attention in recent years due to their high gain, wide BW, simple fabrication process, and zero-conductor losses [25], [26]. However, one of the biggest challenges for dielectric reflectarrays is to reduce the size. The authors of [27] use an array of flat, foldable unit cells to achieve a high-performance, deployable dielectric reflectarray that can be folded to 1/3 of the full-scale volume, as indicated in Figure 18. The 3D-printed flexible elastomer enables a novel "snapping-like" mechanism that can be folded and deployed effortlessly using a single-shot deployment technique. Table 1 presents a performance comparison of the state-of-the-art dielectric reflectarrays operating at similar frequency ranges using three different manufacturing methods. The additively manufactured, 3D-printed, origami-inspired reflectarray shows superior performance, offering design deployability and a realized BW of 16%. The origami benefits and high performance make it an ideal candidate for applications such as 5G mobile stations, agricultural base stations, and satellite communications.

5G RFIDs

With the massive increase in the number of IoT devices to be installed during the next couple of years, there is an urgent need to equip them with harvesting, communication, and high-accuracy localization capabilities and to manufacture them using low-cost and environmentally friendly processes. The following sections cover system-level breakthroughs in the field of 5G and mm-wave energy, enabling up to hundreds of meters in harvesting, kilometer range in communication, and down to hundreds of μm in localization accuracy.

Extended-Range Operation

Modular antenna arrays can be more easily realized at mm-wave frequencies, enabling a wider range of scalability for their antenna aperture. However, with the increase in antenna gain comes the inability to provide isotropic angular coverage, translating to a loss in communication link when the Rx is not properly steered toward the source of power. One solution to mitigate this problem is the implementation of beamforming networks (BFNs), which are used to effectively create simultaneous beam-angular coverage with large-gain arrays by mapping a set of directions to a set of feeding ports.

The Rotman lens, introduced in the 1960s, is a unique type of passive BFN that introduces true time delays (TTDs) to wavefronts impinging on its various surface ports [30]. A significant advantage resulting from TTDs is the ultrawideband operation, which differentiates the Rotman lens from any other passive BFN, such as the butler or blass matrices, which exhibit
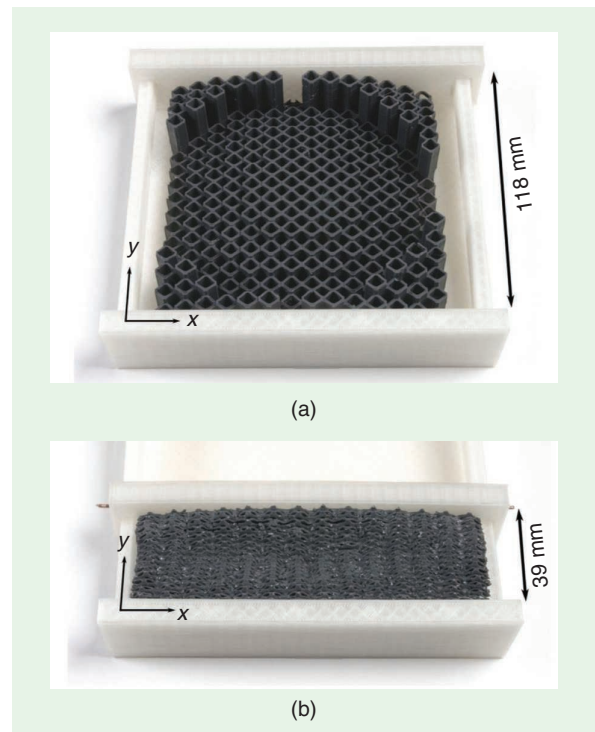
Figure 18. *A fabricated origami-inspired deployable dielectric reflectarray. (a) The front-side view of a fully deployed sample and (b) the back-side view of a fully retracted sample [27].*

TABLE 1. A comparison with the state-of-the-art dielectric reflectarrays using different fabrication methods.

Design	Fabrication	Frequency (GHz)	Size (λ^2)	Gain (dB)	BW (%)	Deploys
[28]	PCB etching	35	153.9	23.9	N/A	No
[29]	Monolithic	31	154	28.3	5	No
[27]	3D printing	29	129.3	25.5	16	Yes

PCB: printed circuit board; N/A: not applicable.

much narrower BWs. As for its geometry, the Rotman lens is a structure with two angles of curvatures supporting antenna ports on one side and beam ports on the opposite side [31].

With proper tuning of the lens' parameters according to the geometrical optics approximation, the plane waves impinging on the antenna side of the lens are focused to different focal points on the beam-ports side of the lens. Varying the number of antenna and beam ports has an effect on the array factor and angular coverage of the Rotman lens. This effect was studied by designing structures of varying sizes at 28 GHz using Antenna Magus before simulation in CST Studio Suite 2018. An optimal compromise between a high array factor of 5.95 dB and a 120° total angular coverage was observed for a set of eight antenna arrays and six beam ports while maintaining a reasonable number of ports. After finalizing the design of the lens, eight antenna arrays consisting of five serially fed patch antennas were then added to its antenna ports [32]. The ports' E-plane beamwidth of roughly 18° (provided by the five antennas) is appropriate for a majority of use cases

Figure 19. *The (a) flexible Rotman lens-based antenna array and (b) measured and simulated gain values at all six ports (P1–P6) of the Rotman lens-based antenna array [33].*

where environments expand mostly horizontally. The design was then printed on flexible copper-clad liquid crystal polymer (LCP) substrate ($e_r = 3.02$ and $h = 180\,\mu m$) using an inkjet-printed masking technique followed by etching, resulting in the structure shown in Figure 19(a), which was mounted on a 1.5-in radius cylinder.

The radiation properties of the lens-based antenna system were simulated and accurately measured at every port, while all five remaining ports were terminated with a 50-Ω load to ensure the proper operation of the lens. The lens antenna array was precisely rotated in angular increments of 5° while being illuminated with a 20-dBi horn antenna. Both the simulated and measured gains are presented in Figure 19(b), displaying very good similarity and demonstrating a measured gain of approximately 17 dBi and an angular coverage of roughly 110° in front of the lens, thereby validating the effective operation of the antenna array.

5G: A Wireless Power Grid for the IoT

EM energy harvesting offers numerous solutions related to the current booming need for power-autonomous, low-cost IoT devices. The literature is packed with research targeting low frequencies—UHF and RF bands—as sources of ambient power [34]–[36]. Compared to their lower-frequency counterparts, fewer implementations are presented in the literature targeting energy harvesting at higher frequencies, more specifically, 24 GHz and above, where, as mentioned previously, higher-transmitted powers up to 75 dBm are available. However, these systems, [37]–[39], suffer from narrow angular coverage. To take advantage of this high EIRP available at 5G, the Rotman lens, presented in the "Extended-Range Operation" section, was used to enable high-efficiency, wide angular-coverage mm-wave harvesting. Because the lens is capable of focusing the energy coming from a given direction into its geometrically associated beam port, gallium arsenide diode-based rectifiers were connected at these ports followed by a dc-combining stage (based on bypass diodes) to collect the dc output independent of the direction of the incoming wave.

To assess the value of the Rotman lens addition, a reference structure, excluding the Rotman lens and comprising eight parallel rectennas (and, therefore, eight diodes), was designed and printed, as shown in Figure 20(b). A direct serial-combining network was implemented with the non-Rotman-based rectenna because all of the rectifiers in this structure are expected to be excited at the same time, unlike the Rotman-based rectenna where, ideally, one rectifier will be on at a time. The two rectennas (Rotman and non-Rotman-based) were characterized as a function
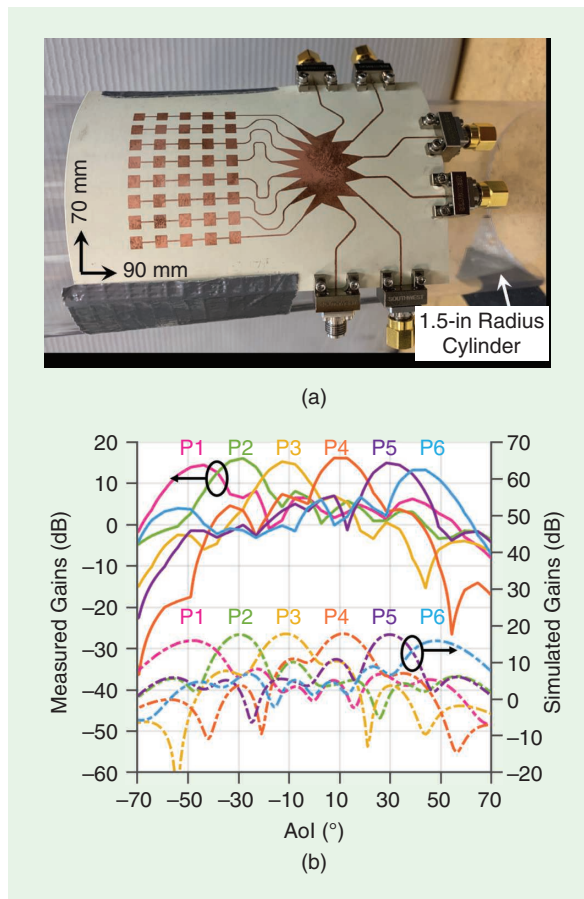
of their received power density, as depicted in Figure 20(c), where the harvested voltages and powers of both arrays are plotted. It can be observed that, at low power levels (where small increments in the RF power level translate to large differences in the efficiency of the rectifiers), the differences between the two arrays are very pronounced; the Rotman lens-based rectenna demonstrates an enhanced sensitivity, with a 6-dB lower turn-on power density compared to its non-Rotman counterpart [32].

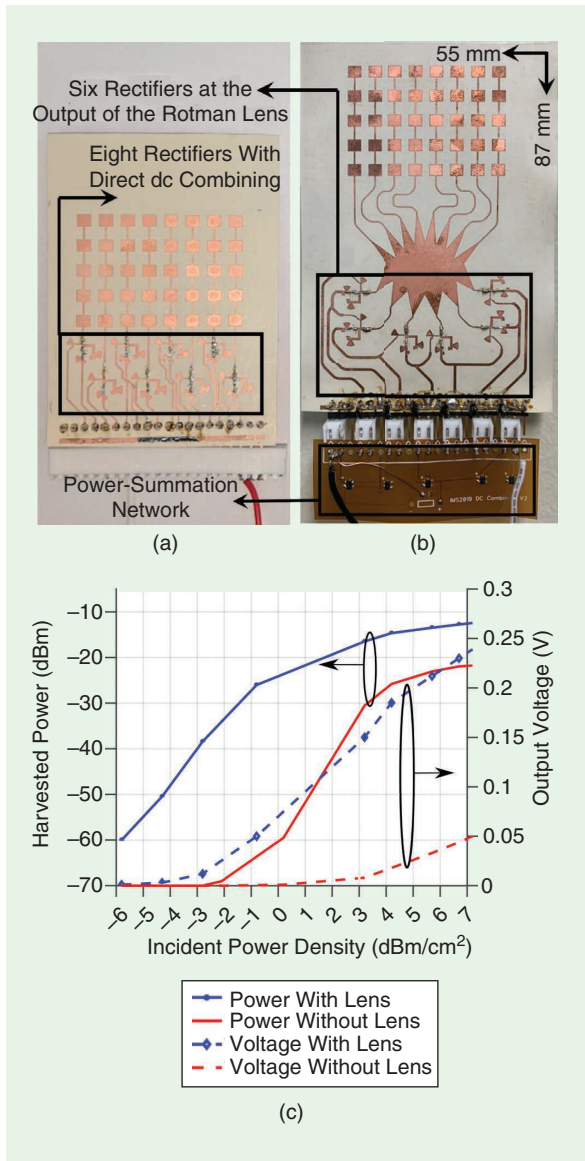Tested with respect to different AoIs, the Rotman-based rectenna's average harvested powers (in natural scale) demonstrated a 21-fold gain relative to that of its simple counterpart. With such enhanced turn-on power densities resulting from the lens' internal RF combining and equipped with rectifiers having sensitivities down to –30 dBm, such as the one presented in [40], [41], harvesting ranges in excess of 150 m can be achieved under the allowed 75-dBm EIRP at 5G.

5G: A Potential Gateway for the Battery-Less IoT

The "5G: A Wireless Power Grid for the IoT" section demonstrated the successful implementation of the Rotman lens for high-gain and large-beamwidth mm-wave energy harvesting. If the Rotman lens structure could be equipped with backscattered communication capabilities, then the door for high-beamwidth and high-gain fully passive RFIDs would be open. In addition to the advantage of RF combining enabled by the lens, the lens is also not limited to amplitude-modulation schemes. By simply changing the load at all the beam ports, the modulation of the reflection can be implemented, and the techniques applied to traditional lower-frequency RFIDs, including continuous spectrally efficient modulation [42], can also be exploited.

To build a Rotman lens-based retrodirective structure, six low-cost mm-wave switches were added to the beam ports of the structure presented in Figure 19(a) [33]. The monostatic differential radar cross section (RCS) of the resulting structure was measured using two co-located emitting and receiving horn antennas, while the array was placed on planar and bent surfaces and precisely rotated in angular increments of 5°. By controlling the biasing on the switches connected at the beam ports, the ON and OFF RCSs were measured, and their difference was later calculated to extract the differential RCS of the structure. A reference target—a 6-in-radius metal sphere—was used for the accurate normalization of the RCS measurements. Figure 21

Figure 20. *(a) The simple rectenna design and (b) the Rotman-based rectenna. (c) A plot of the measured voltages and output powers versus the incident power density for the rectenna with and without a Rotman lens [32].*
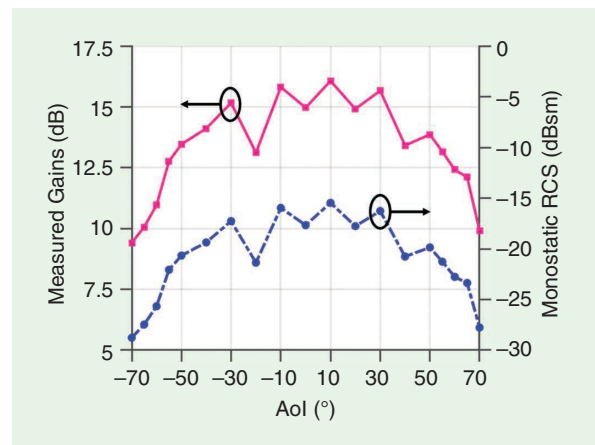

Figure 21. *A plot of the measured monostatic differential RCS as well as the extracted gain of the Rotman-based retrodirective front end [33].*

displays the monostatic differential RCS as well as the associated gain of the Rotman lens-based retrodirective array placed on a planar surface.

The results of this test, measured at an optimal frequency of 28.5 GHz, display a maximum RCS of –15.4 dBsm with a variation lower than 8 dB over 120° of interrogation angle. The Rotman lens retrodirective array offers a high and largely isotropic monostatic differential RCS. The RCS behavior was also tested under bending, when the lens was placed on cylinders with radii ranging 1.5–2.5 in. It was observed that the printed and flexible mm-wave Rotman lens maintains a stable and robust performance under bending, with a measured variation of the RCS lower than 8 dB (corresponding to 4 dB in gain) over its entire angular coverage [33].

To build the entire RFID and test its long-range communication capabilities, a low-power oscillator, voltage regulator, and flexible solar cell were added to the Rotman-based retrodirective structure. The overall power consumption of the system was measured to be 2.64 μW, effortlessly supplied by the attached solar cell under normal indoor-office lighting conditions. The tag was placed at various distances in an indoor hallway away from the reader, which was transmitting

Figure 22. *(a) The layout of the proposed RFID tag showing the RF front end and baseband components. (b) The fabricated, miniaturized RFID tag [44].*

48-dBm EIRP. In such an environment, this system would allow for a maximum reading range of 179 m. It should be noted that the noise floor here is limited by the amount of phase-noise coupling from the Tx to the Rx. With an improved isolation bringing their coupling to the thermal noise floor, maximum outdoor ranges of 780 m and 1.8 km could be achieved with 48 dBm and the 75-dBm maximum allowed for 5G base-station EIRPs, respectively.

AM-Enabled mm-Wave RFID for Spatial Localization in IoT Applications

Backscatter communication presents itself as a particularly attractive means of communication, consistent with the need and desire for long-lasting, perpetual IoT devices and sensor nodes. Developed in the late 1940s as "communication by means of reflected power," it involves the modulation and subsequent reflection of an illuminating RF carrier signal. Consequently, energy consumption occurs in only one half of the communication link, as any required bits of information can be encoded in the modulated and reflected signal. This enables reliable communication links to be maintained with an instantaneous power consumption lower than 1 μW [43].

As highlighted in the "5G: A Potential Gateway for the Battery-Less IoT" section and in [45], large, high-gain RCS structures such as the Van Atta array and Rotman lens operating at mm-wave frequencies enable the development of low-power, ultralong-range mm-wave RFIDs. Taking this a bit further and fully utilizing the advantages that come with adopting mm-wave frequencies, which enable very low form-factor devices, miniaturized mm-wave RFID tags can be developed for use as high-performance wireless modules in short-range (<10-m) IoT applications. An RFID tag proposed in [44] consists of an RF front end, which is made up of a cross-polarized rectangular patch antenna and a single RF transistor to enable backscatter modulation by load switching between an open and short circuit termination. The baseband of the proposed tag includes a low-power oscillator, voltage regulator, and super capacitor, which provides an energy-storage element. The tag is designed to operate in the 24-GHz industry, science, and medicine (ISM) frequency band. Figure 22(a) shows the layout of the proposed RFID tag, indicating the RF front end and baseband components. The tag is fabricated using an inkjet masking process, where a photoresist is printed onto the copper-clad surface of a flexible LCP substrate (e_r = 3.14 and h = 180 μm) followed by etching. The fabricated device is displayed in Figure 22(b).

In a dense implementation of these devices and sensor nodes, which is typically desired, it is imperative to develop a scheme to simultaneously and seamlessly
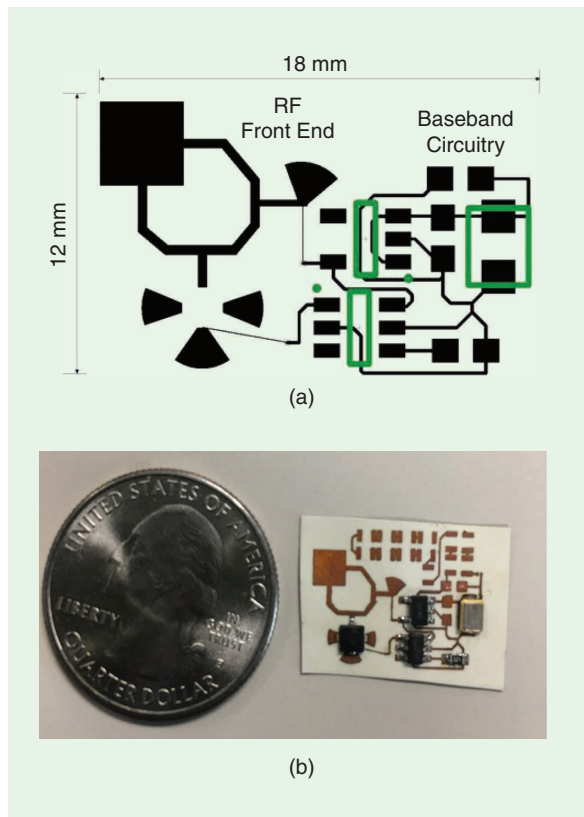
interrogate and aggregate useful information from a cluster of these devices. A standout means of achieving this, one that has gained increasing popularity over the last few years, is frequency-modulated continuous-wave (FMCW) radar. FMCW radars have gained widespread acceptance particularly at mm-wave frequencies of interest, and there exists a plethora of low-cost, commercially available chip sets and modules that make their deployment tractable [46].

The theory of operation of FMCW radar, at its core, is relatively simple: a continuous wave with a time-varying frequency is sent by the Tx, and, after reflection from a target at a given distance, a delayed and attenuated copy of the transmitted signal is received. The auto-correlation of the transmitted and received signals is produced using a mixer that generates two signals: one with a phase that is the sum of the phases (sum signal) of the correlated signals and one with a phase equal to the difference of the phases (difference signal) [47]. The sum signal generally represents a high-frequency component of the baseband signal and is filtered out using a low-pass filter. The resultant signal, also known as the *beat signal*, contains the required information and is passed on for further processing. In conventional FMCW applications, the beat signal is simply a function of the distance between a target and the radar; however, due to the active nature of the target in this case, the beat signal is modulated and, consequently, is one of the primary advantages of utilizing a modulated backscatter approach in conjunction with FMCW radar. Generally, nearby reflectors and the self-coupling between the Tx and Rx channels of the radar generate low-frequency components around dc, which would drown out a passive target; with this approach, however, the beat signal can be shifted away from the clutter, as illustrated in Figure 23.

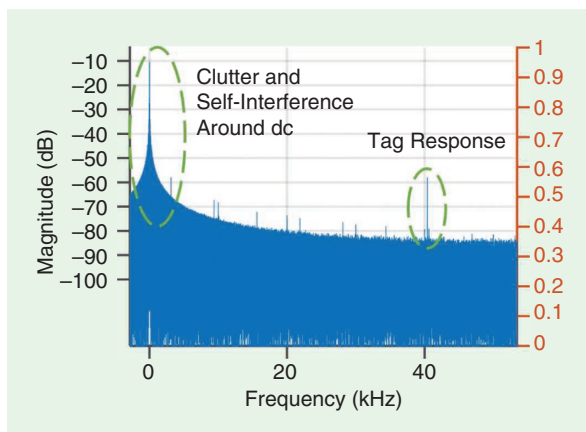In most IoT sensor applications, it becomes imperative to obtain, with high fidelity, the spatial location from which specific sensor information emanates. The localization information comes in two pieces: the range of the target and the angle of arrival with respect to the reader. The range is easily determined from the beat frequency of the backscattering target, although the BW and signal-to-noise ratio limitations impose a bottleneck on the achievable accuracy of localization. This is overcome by employing mathematical interpolation over the raw frequency-domain information to achieve centimeter-level accuracy. Further phase evaluation can be done to improve accuracy and has been shown extensively in the literature for passive targets achieving submillimeter accuracy. To obtain a complete spatial picture, it is necessary to resolve the angular location of the tag. This is achieved by making use of a receiving antenna array with at least two elements to sample the received signal. The angle of arrival is obtained as a function of the difference in phase among the received antenna elements due to the extra path length the wave travels relative to each receiving antenna element. Figure 24 shows the processed return for a tag at boresight of the reader.

The described technology, in combination with AM techniques such as inkjet printing, presents a strong outlook for the future in the development of densely implemented, low-cost, low-power, low form-factor, and localizable high-performance wireless modules for use in IoT applications. There have been myriad efforts reporting the use of FMCW radar-based detection with active backscatter modulating RFID tags for use in localization and detection. However, many of these methods, such as those in [48]–[50], present transponders with fairly large form factors and high power consumption as a result of increasing design complexity at the reader and the tag as well as more intensive digital signal processing to extract the required information.
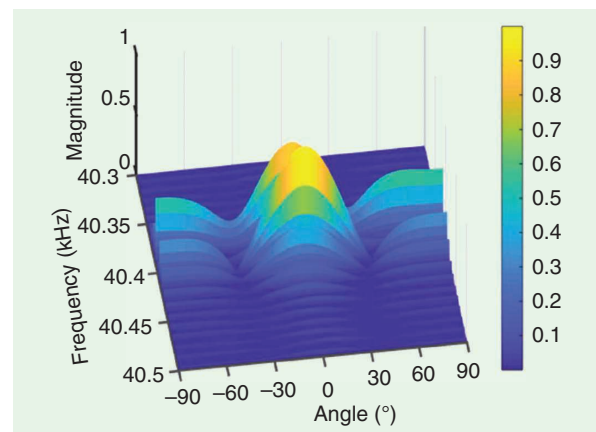

Figure 23. *The baseband FMCW radar return showing a clutter and modulated backscatter response [44].*

Figure 24. *The tag response at 0° with respect to the reader [44].*

Conclusions

This article highlighted innovative topologies that incorporate AM techniques including inkjet, 3D, and 4D printing to achieve designs that demonstrate new levels of performance for mm-wave applications relevant to next-generation systems. The manufacturing technology demonstrates the ability to become more than just an alternative method of fabrication focused on rapid prototyping, concentrating instead on enabling new designs that represent state-of-the-art performance in their domains of operation [51]. The described designs improve the various stages of mm-wave communication and enable novel systems for next-generation IoT devices operating in 5G+, including improved interconnects for reduced packaging losses in an MCM, smart packaging incorporating similar interconnects to improve compact energy harvesting for perpetual IoT, and novel reflectarray and FSS structures to improve gain and noise rejection. These improvements are developed in conjunction with novel mm-wave RF architectures that directly benefit from integration, including Rotman lens-based arrays for energy harvesting and retrodirective RFID front ends, as well as modulated mm-wave backscatter RFID tags for FMCW radar.

These architectures are vital for improving key aspects in the fields in which mm-wave is poised to dominate, specifically where phased arrays are expected to be utilized for scanning everything from cluttered city and indoor environments to long-range agricultural applications. The topologies demonstrate enhancements in critical parameters at mm-wave frequencies, including both improved energy harvesting and backscatter RFIDs for extended ranges and AoI, as well as improvements in modulated RFIDs for cluttered environments. These technologies offer unprecedented development focused on applications that are becoming rapidly viable with the upcoming shift to widespread use of mm-wave devices.

Acknowledgments

References

[1] B. Tehrani, C. Mariotti, B. S. Cook, L. Roselli, and M. M. Tentzeris, "Development, characterization, and processing of thin and thick inkjet-printed dielectric films," *Organ. Electron.*, vol. 29, pp. 135–141, 2016. doi: 10.1016/j.orgel.2015.11.022.

[2] A. Nathan et al., "Flexible electronics: The next ubiquitous platform," *Proc. IEEE*, vol. 100, no. Special Centennial Issue, pp. 1486–1517, 2012. doi: 10.1109/JPROC.2012.2190168.

[3] M. T. Craton, J. D. Albrecht, P. Chahal, and J. Papapolymerou, "A chip-first approach to millimeter-wave circuit packaging," *IEEE Microw. Wireless Compon. Lett.*, vol. 29, no. 2, pp. 1–3, 2019. doi: 10.1109/LMWC.2018.2886737.

[4] C. Armiento, S. Trulli, A. Akyurtlu, E. Harper, M. Haghzadeh, and C. Laighton, "Printed electronics and additive packaging for microwave applications," in *Proc. Int. Conf. Electron. Packag. (ICEP)*, Apr. 2017, pp. 1–2. doi: 10.23919/ICEP.2017.7939309.

[5] T. Merkle, R. Gtzen, J. Choi, and S. Koch, "Polymer multichip module process using 3-d printing technologies for d-band applications," *IEEE Trans. Microw. Theory Techn.*, vol. 63, no. 2, pp. 481–493, Feb. 2015. doi: 10.1109/TMTT.2014.2387823.

[6] T. Merkle and R. Gtzen, "Millimeter-wave surface mount technology for 3-D printed polymer multichip modules," *IEEE Trans. Compon. Packag. Manuf. Technol.*, vol. 5, no. 2, pp. 201–206, Feb. 2015. doi: 10.1109/TCPMT.2014.2387232.

[7] T. Krems, W. Haydl, H. Massler, and J. Rudiger, "Millimeter-wave performance of chip interconnections using wire bonding and flip chip," in *Proc. IEEE MTT-S Int. Microw. Symp. Dig.*, vol. 1, June 1996, pp. 247–250. doi: 10.1109/MWSYM.1996.508504.

[8] X. He, B. K. Tehrani, R. Bahr, W. Su, and M. M. Tentzeris, "Additively manufactured mm-wave multichip modules with fully printed 'smart' encapsulation structures," *IEEE Trans. Microw. Theory Techn.*, vol. 68, no. 7, pp. 1–9, 2019. doi: 10.1109/TMTT.2019.2956934.

[9] Y. Cui, W. Su, and M. M. Tentzeris, "Fully inkjet-printed tunable flexible microfluidic chipless RFID sensor," in *Proc. 2019 Int. Appl. Comput. Electromagn. Soc. Symp. (ACES)*, pp. 1–2.

[10] J. Hester, "Low cost printed, flexible, and energy autonomous van-atta and carbon-nanotubes-based mm-wave RFID gas sensors for ultra-long-range ubiquitous IoT and 5G implementations," Ph.D. dissertation, Georgia Inst. Technol, 2019.

[11] T. Lin, J. Bito, J. G. D. Hester, J. Kimionis, R. A. Bahr, and M. M. Tentzeris, "On-body long-range wireless backscattering sensing system using inkjet-/3-D-printed flexible ambient RF energy harvesters capable of simultaneous DC and harmonics generation," *IEEE Trans. Microw. Theory Techn.*, vol. 65, no. 12, pp. 5389–5400, 2017. doi: 10.1109/TMTT.2017.2768033.

[12] T. Lin, W. Su, and M. M. Tentzeris, "Expand horizons of microfluidic systems: An inkjet printed flexible energy autonomous micropump system for wearable and IoT microfluidic applications," in *Proc. 2018 IEEE/MTT-S Int. Microw. Symp. - IMS*, pp. 812–815. doi: 10.1109/MWSYM.2018.8439441.

[13] T. Lin, S. N. Daskalakis, A. Georgiadis, and M. M. Tentzeris, "Achieving fully autonomous system-on-package designs: An embedded-on-package 5G energy harvester within 3D printed multilayer flexible packaging structures," in *Proc. IEEE MTT-S Int. Microw. Symp. (IMS)*, 2019, pp. 1375–1378. doi: 10.1109/MWSYM.2019.8700931.

[14] T. Lin, R. Bahr, M. M. Tentzeris, P. M. Raj, V. Sundaram, and R. Tummala, "Novel 3D-/inkjet-printed flexible on-package antennas, packaging structures, and modules for broadband 5G applications," in *Proc. 2018 IEEE 68th Electron. Compon. Technol. Conf. (ECTC)*, pp. 214–220. doi: 10.1109/ECTC.2018.00041.

[15] T.-H. Lin, R. A. Bahr, and M. M. Tentzeris, *Additive Manufacturing AiP Designs and Applications*. Hoboken, NJ: Wiley, 2020, ch. 9, pp. 267–291. [Online]. Available: https://onlinelibrary.wiley.com/doi/abs/10.1002/9781119556671.ch9

[16] B. K. Tehrani, R. A. Bahr, W. Su, B. S. Cook, and M. M. Tentzeris, "E-band characterization of 3D-printed dielectrics for fully-printed millimeter-wave wireless system packaging," in *Proc. 2017 IEEE MTT-S Int. Microwave Symp. (IMS)*, pp. 1756–1759. doi: 10.1109/MWSYM.2017.8058985.

[17] D. Liu, X. Gu, C. W. Baks, and A. Valdes-Garcia, "Antenna-in-package design considerations for Ka-band 5G communication applications," *IEEE Trans. Antennas Propag.*, vol. 65, no. 12, pp. 6372–6379, 2017. doi: 10.1109/TAP.2017.2722873.

[18] H. Kim et al., "A 28Ghz CMOS direct conversion transceiver with packaged antenna arrays for 5G cellular system," in *Proc. 2017 IEEE Radio Freq. Integr. Circuits Symp. (RFIC)*, pp. 69–72. doi: 10.1109/RFIC.2017.7969019.

[19] X. Gu et al., "Development, implementation, and characterization of a 64-element dual-polarized phased-array antenna module for 28-Ghz high-speed data communications," *IEEE Trans. Microw. Theory Techn.*, vol. 67, no. 7, pp. 2975–2984, 2019. doi: 10.1109/TMTT.2019.2912819.

[20] A. Nafe, M. Sayginer, K. Kibaroglu, and G. M. Rebeiz, "2x64 dual-polarized dual-beam single-aperture 28 Ghz phased array with high cross-polarization rejection for 5G polarization MIMO," in *Proc. IEEE MTT-S Int. Microw. Symp. (IMS)*, 2019, pp. 484–487.

[21] Y. Huo, X. Dong, and W. Xu, "5G cellular user equipment: from theory to practical hardware design," *IEEE Access*, vol. 5, pp. 13,992–14,010, July 2017. doi: 10.1109/ACCESS.2017.2727550.

[22] S. A. Nauroze, L. S. Novelino, M. M. Tentzeris, and G. H. Paulino, "Continuous-range tunable multilayer frequency-selective surfaces using origami and inkjet printing," *Proc. Nat. Acad. Sci.*, vol. 115, no. 52, pp. 13,210–13,215, 2018. doi: 10.1073/pnas.1812486115.

[23] K. Fuchi, J. Tang, B. Crowgey, A. R. Diaz, E. J. Rothwell, and R. O. Ouedraogo, "Origami tunable frequency selective surfaces," *IEEE Antennas Wireless Propag. Lett.*, vol. 11, pp. 473–475, Apr. 2012. doi: 10.1109/LAWP.2012.2196489.

[24] Y. Cui, S. A. Nauroze, and M. M. Tentzeris, "Novel 3d-printed reconfigurable origami frequency selective surfaces with flexible ink-jet-printed conductor traces," in *Proc. 2019 IEEE MTT-S Int. Microw. Symp. (IMS)*, pp. 1367–1370. doi: 10.1109/MWSYM.2019.8700994.

[25] P. Nayeri et al., "3d printed dielectric reflectarrays: Low-cost high-gain antennas at sub-millimeter waves," *IEEE Trans. Antennas Propag.*, vol. 62, no. 4, pp. 2000–2008, 2014. doi: 10.1109/TAP.2014.2303195.

[26] F. Yang et al., "Reflectarray design at infrared frequencies: Effects and models of material loss," *IEEE Trans. Antennas Propag.*, vol. 60, no. 9, pp. 4202–4209, 2012. doi: 10.1109/TAP.2012.2207029.

[27] Y. Cui, R. Bahr, S. A. Nauroze, and M. M. Tentzeris, "3D printed one-shot deployable flexible 'kirigami' dielectric reflectarray antenna for mm-wave applications," in *Proc. IEEE MTT-S Int. Microw. Symp. (IMS)*, 2020.

[28] Y. Sun and K. W. Leung, "Millimeter-wave substrate-based dielectric reflectarray," *IEEE Antennas Wireless Propag. Lett.*, vol. 17, no. 12, pp. 2329–2333, Dec. 2018. doi: 10.1109/LAWP.2018.2874082.

[29] M. h Jamaluddin et al., "Design, fabrication and characterization of a dielectric resonator antenna reflectarray in Ka-band," *Prog. Electromagn. Res. B*, vol. 25, no. 25, pp. 261–275, 2010. doi: 10.2528/PIERB10071306.

[30] R. Rotman, M. Tur, and L. Yaron, "True time delay in phased arrays," *Proc. IEEE*, vol. 104, no. 3, pp. 504–518, 2016. doi: 10.1109/JPROC.2016.2515122.

[31] W. Rotman and R. Turner, "Wide-angle microwave lens for line source applications," *IEEE Trans. Antennas Propag.*, vol. 11, no. 6, pp. 623–632, 1963. doi: 10.1109/TAP.1963.1138114.

[32] A. Eid, J. Hester, and M. M. Tentzeris, "A scalable high-gain and large-beamwidth mm-wave harvesting approach for 5G-powered IoT," in *Proc. IEEE MTT-S Int. Microw. Symp. (IMS)*, June 2019, pp. 1309–1312. doi: 10.1109/MWSYM.2019.8700758.

[33] A. Eid, J. G. Hester, and M. M. Tentzeris, "Rotman lens-based wide angular coverage and high gain semi-passive architecture for ultra-long range mm-wave RFIDs," *IEEE Antennas Wireless Propag. Lett.*, early access, 2020. doi: 10.1109/LAWP.2020.3002924.

[34] S. Kim et al., "Ambient RF energy-harvesting technologies for self-sustainable standalone wireless sensor platforms," *Proc. IEEE*, vol. 102, no. 11, pp. 1649–1666, 2014. doi: 10.1109/JPROC.2014.2357031.

[35] Z. Liu, Z. Zhong, and Y.-X. Guo, "Enhanced dual-band ambient RF energy harvesting with ultra-wide power range," *IEEE Microw. Compon. Lett.*, vol. 25, no. 9, pp. 630–632, 2015. doi: 10.1109/LMWC.2015.2451397.

[36] W. Zahra and T. Djerafi, "Ambient RF energy harvesting for dual-band frequencies below 6 GHz," in *Proc. 2018 IEEE Wireless Power Transfer Conf. (WPTC)*, pp. 1–2. doi: 10.1109/WPT.2018.8639488.

[37] J. Bito et al., "Millimeter-wave ink-jet printed RF energy harvester for next generation flexible electronics," in *Proc. Wireless Power Transfer Conf. (WPTC)*, 2017, pp. 1–4. doi: 10.1109/WPT.2017.7953871.

[38] S. Ladan, A. B. Guntupalli, and K. Wu, "A high-efficiency 24 GHz rectenna development towards millimeter-wave energy harvesting and wireless power transmission," *IEEE Trans. Circuits Syst. I: Reg. Papers*, vol. 61, no. 12, pp. 3358–3366, 2014. doi: 10.1109/TCSI.2014.2338616.

[39] A. Okba, A. Takacs, H. Aubert, S. Charlot, and P.-F. Calmon, "Multiband rectenna for microwave applications," *Comptes Rendus Phys.*, vol. 18, no. 2, pp. 107–117, 2017. doi: 10.1016/j.crhy.2016.12.002.

[40] A. Eid, J. Hester, B. Tehrani, and M. Tentzeris, "Flexible w-band rectifiers for 5G-powered IoT autonomous modules," in *Proc. 2019 IEEE Int. Symp. Antennas Propag. USNC-URSI Radio Sci. Meeting*, pp. 1163–1164. doi: 10.1109/APUSNCURSINRSM.2019.8888600.

[41] A. Eid, J. Hester, and M. Tentzeris, "mm-wave tunnel diode-based rectifier for perpetual IoT," in *Proc. 2020 IEEE Int. Symp. Antennas Propag. USNC-URSI Radio Sci. Meeting*.

[42] J. Kimionis and M. M. Tentzeris, "Pulse shaping: The missing piece of backscatter radio and RFID," *IEEE Trans. Microw. Theory Techn.*, vol. 64, no. 12, pp. 4774–4788, 2016. doi: 10.1109/TMTT.2016.2623703.

[43] J. G. D. Hester, J. Kimionis, R. Bahr, W. Su, B. Tehrani, and M. M. Tentzeris, "Radar additive manufacturing technologies: The future of Internet of Things (IoT)," in *Proc. IEEE Radar Conf. (RadarConf18)*, Apr. 2018, pp. 0447–0452. doi: 10.1109/RADAR.2018.8378600.

[44] A. O. Adeyeye, J. Hester, and M. M. Tentzeris, "Miniaturized millimeter wave RFID tag for spatial identification and localization in Internet of Things applications," in *Proc. 2019 49th Euro. Microw. Conf. (EuMC)*, pp. 105–108. doi: 10.23919/EuMC.2019.8910740.

[45] J. G. Hester and M. M. Tentzeris, "A mm-wave ultra-long-range energy-autonomous printed RFID-enabled van-atta wireless sensor: At the crossroads of 5G and IoT," in *Proc. 2017 IEEE MTT-S Int. Microw. Symp. (IMS)*, pp. 1557–1560. doi: 10.1109/MWSYM.2017.8058927.

[46] J. Lien et al., "Soli: Ubiquitous gesture sensing with millimeter wave radar," *ACM Trans. Graph. (TOG)*, vol. 35, no. 4, pp. 1–19, 2016. doi: 10.1145/2897824.2925953.

[47] R. Sorrentino, E. Sbarra, L. Urbani, S. Montori, R. V. Gatti, and L. Marcaccioli, "Accurate FMCW radar-based indoor localization system," in *Proc. IEEE Int. Conf. RFID-Technol. Appl. (RFID-TA)*, Nov. 2012, pp. 362–368. doi: 10.1109/RFID-TA.2012.6404547.

[48] A. Strobel, C. Carlowitz, R. Wolf, F. Ellinger, and M. Vossiek, "A millimeter-wave low-power active backscatter tag for FMCW radar systems," *IEEE Trans. Microw. Theory Techn.*, vol. 61, no. 5, pp. 1964–1972, 2013. doi: 10.1109/TMTT.2013.2252915.

[49] M. Vossiek and P. Gulden, "The switched injection-locked oscillator: A novel versatile concept for wireless transponder and localization systems," *IEEE Trans. Microw. Theory Techn.*, vol. 56, no. 4, pp. 859–866, 2008. doi: 10.1109/TMTT.2008.918158.

[50] K. Wang, J. Gu, F. Ren, and K. Wu, "A multitarget active backscattering 2-D positioning system with superresolution time series post-processing technique," *IEEE Trans. Microw. Theory Techn.*, vol. 65, no. 5, pp. 1751–1766, 2017. doi: 10.1109/TMTT.2017.2660481.

[51] A. Eid, J. Hester, Y. Fang, B. Tehrani, S. A. Nauroze, R. Bahr, and M. M. Tentzeris, "Nanotechnology-empowered flexible printed wireless electronics: A review of various applications of printed materials," *IEEE Nanotechnol. Mag.*, vol. 13, no. 1, pp. 18–29, 2018. doi: 10.1109/MNANO.2018.2869233.